ACS APPLIED MATERIALS & INTERFACES

Research Article

www.acsami.org

Self-Assembly of Large Gold Nanoparticles for Surface-Enhanced Raman Spectroscopy

Guang Yang,[†,‡,∥] Jagjit Nanda,[⊥] Boya Wang,[†,§] Gang Chen,[†,§] and Daniel T. Hallinan, Jr.*[,†,‡,∥]

[†]Aero-propulsion, Mechatronics, and Energy Center, Florida State University, Tallahassee, Florida 32310, United States

[‡]Chemical and Biomedical Engineering Department and [§]Civil & Environmental Engineering Department, Florida A&M University-Florida State University College of Engineering, Tallahassee, Florida 32310, United States

[∥]The National High Magnetic Field Laboratory, Florida State University, Tallahassee, Florida 32310, United States

[⊥]Materials Science and Technology Division, Oak Ridge National Laboratory, Oak Ridge, Tennessee 37831, United States

Supporting Information

ABSTRACT: Performance of portable technologies from mobile phones to electric vehicles is currently limited by the energy density and lifetime of lithium batteries. Expanding the limits of battery technology requires *in situ* detection of trace components at electrode−electrolyte interphases. Surface-enhance Raman spectroscopy could satisfy this need if a robust and reproducible substrate were available. Gold nanoparticles (Au NPs) larger than 20 nm diameter are expected to greatly enhance Raman intensity if they can be assembled into ordered monolayers. A three-phase self-assembly method is presented that successfully results in ordered Au NP monolayers for particle diameters ranging from 13 to 90 nm. The monolayer structure and Raman enhancement factors (EFs) are reported for a model analyte, rhodamine, as well as the best performing polymer electrolyte salt, lithium bis(trifluoromethane)sulfonimide. Experimental EFs for the most part correlate with predictions based on monolayer geometry and with numerical simulations that identify local electromagnetic field enhancements. The EFs for the best performing Au NP monolayer are between 10^6 and 10^8 and give quantitative signal response when analyte concentration is changed.

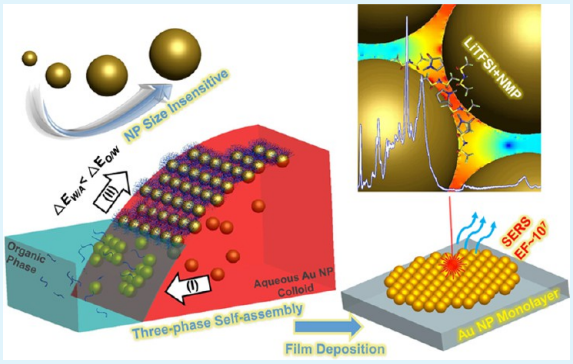

KEYWORDS: *surface-enhanced Raman spectroscopy, gold nanoparticle, self-assembly, monolayer, battery electrolyte, FDTD*

INTRODUCTION

Surface-enhanced Raman spectroscopy (SERS) exhibits considerably magnified vibrational signatures of extremely low concentration molecules.[1,2] This opens new avenues for rapid and sensitive detection of analytes in numerous fields such as lithium battery electrodes,[3] catalysis,[4] explosive detection,[5] biosensing,[6−9] and food safety.[10] After years of debate, it is now commonly accepted that the SERS effect primarily originates from coupling of incident laser light with the localized surface plasmon resonance (LSPR) of nanostructured metal surfaces leading to gigantic field enhancement, thereby enhancing the Raman cross section of the analyte.[11] Surface plasmon resonance is the result of collective oscillations of valence electrons in resonance with incident light. It is localized by structures, such as nanoparticles (NPs), whose dimensions are smaller than the wavelength, thus creating a locally amplified electromagnetic (EM) field. The EM field is further enhanced in narrow gaps or regions between NPs due to near-field coupling.[12] Further, this effect is pronounced in NP assemblies that contain surface sites (i.e., hot spots) where the field can be enhanced as much as 100-fold. SERS enhancement can ideally reach a factor of 10^8 as it scales with the EM field to the fourth power. Early efforts of SERS active substrate development were largely focused on rough metal surfaces or random nanoparticle (NP) agglomerates due to the ease for experimental realization.[13] However, the random distribution and orientation of the EM hot spots on those types of SERS substrates cast innumerable hurdles for the reproducible, precise, and quantitative SERS analysis.

Ideally, reproducible SERS substrates would consist of large-scale periodic arrays of hot spots that are consistent through space and stable in time. Two approaches have been taken to fabricate such substrates: "top-down" lithography and other pattering techniques[14−17] and "bottom-up" self-assembly.[18−20] While the former allows accurate control over the geometric nanostructures and hence the SERS response, it suffers from low throughput, high cost, and difficulty in achieving sub-5 nm features. On the other hand, the "bottom-up" approaches allow one to self-assemble metallic NPs into two-dimensional (2D) plasmonic arrays with sub-5 nm interparticle gap in a more

Received: January 22, 2017
Accepted: March 22, 2017
Published: March 22, 2017

DOI: 10.1021/acsami.7b01121
ACS Appl. Mater. Interfaces 2017, 9, 13457−13470

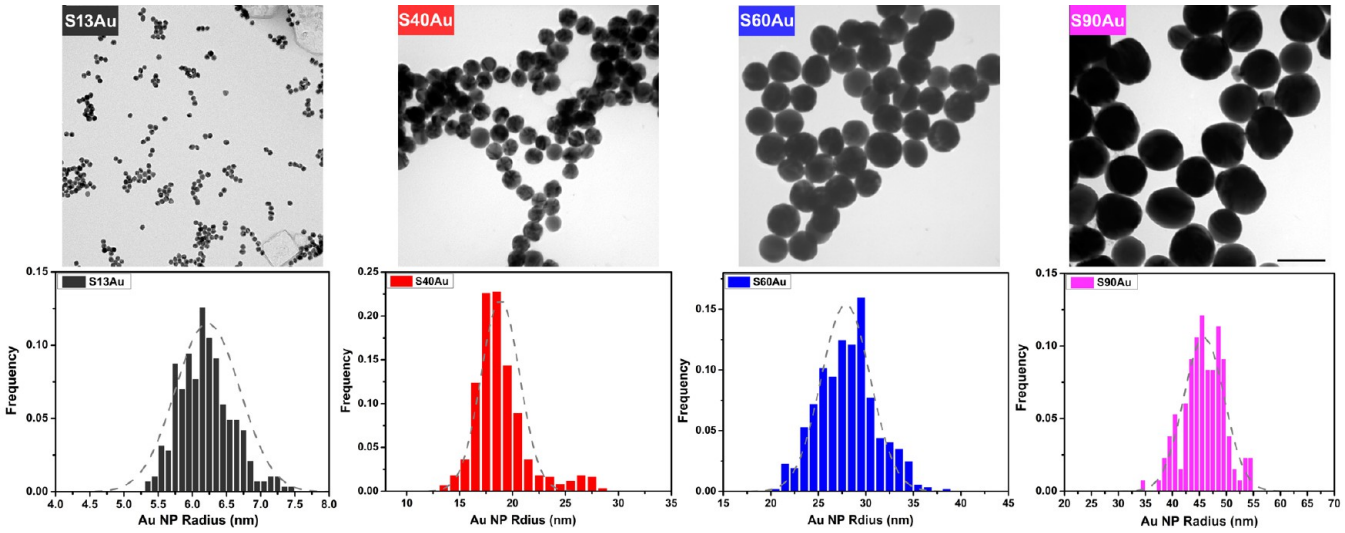

Figure 1. Upper: TEM images of various Au NPs dried from as-synthesized aqueous Au NP colloids. Lower: the corresponding radius histograms with fitted Gaussian distributions (gray dashed line). The scale bar is 100 nm for all TEM images.

Table 1. Related Length Scales of Different Au NP Monolayers

Sample ID	D (nm)	$d_{c\text{-}c}$ (nm)	D/d_{gap}	h (nm)	λ_d (nm)
S13Au	12.7 ± 1.2[a]	15.2 ± 0.1	5.1 ± 0.5	15.4 ± 0.7	14.8 ± 0.3
S40Au	36.7 ± 2.8	38.3 ± 0.5	22.9 ± 1.8	41.5 ± 2.1	39.7 ± 2.0
S60Au	56.0 ± 3.4	59.7 ± 1.0	15.1 ± 1.0	59.3 ± 2.8	57.5 ± 3.7
S90Au	91.7 ± 6.0	93.5 ± 0.8	50.9 ± 3.4	95.4 ± 5.9	93.6 ± 5.3

[a]Note: this value was measured by small-angle X-ray scattering (SAXS).[77]

rapid and cost-effective manner, thus attracting considerable scientific interest in recent years.[11,13,21] These nanoscale gaps are easily controlled with nanoparticle surface functionalization, for example with grafted molecules. With recent developments in nanoparticle assembly, large-scale ordered monolayers can be formed[22] and deposited on solid substrates.[20] Therefore, substrates with regular, reproducible structure are possible. Exceptionally intense EM fields are expected where the hot spots reside,[13] but the exact location and intensity of such hot spots are unknown for large collections of NPs due to EM coupling among the various NPs. This has been practically addressed by immobilizing analytes above but in close proximity to NP monolayers.[23]

As SERS-active nanoscale objects, gold nanoparticles (Au NPs) have been under intensive study due to their ease of synthesis, high Raman sensitivity, and stability.[24] So far, many strategies have been developed in assembling Au NPs into 2D arrays, including drop-casting,[25] electrophoresis deposition,[26,27] Langmuir–Blodgett technique,[28] liquid–liquid interfacial self-assembly,[20,22] and liquid–air interfacial self-assembly.[29] While these self-assembly techniques have been successfully applied to regulate small Au NPs (diameter less than 15 nm) to form 2D periodic arrays, it still remains challenging to self-assemble larger Au NPs into well-ordered large-scale 2D arrays. This is because the long-range van der Waals attractions rapidly increase as the NP size increases whereas the ligand chain mobility decreases on the NP planar facets,[30] leading to the formation of the unmanageable multilayer films or aggregates. Wei et al. overcame this limitation using a custom calixarene-based surfactant of multiple alkylthiol tails.[31] We consider our approach superior due to its versatility. As we show, it is insensitive to NP size and ligand length. The large Au NPs are desired because the optimum size of metallic NPs for maximum SERS enhancement has been found within 20–70 nm,[32] with the SERS enhancement factor (EF) up to 10^7,[33] sufficient for the single molecular detection.[34] To unlock the potential of large Au NPs applied for practical SERS, several approaches have been used to develop a self-assembly strategy for large Au NPs. For example, large NPs have been assembled into 2D arrays at hexane/water interfaces.[35–37] The concentration required to form a monolayer was particle size dependent. Wei et al. designed a calixarene-based surfactant of multiple alkylthiol tails to balance increased van der Waals force for large Au NPs.[31] Despite its simplicity, this method requires crucial choice of custom ligand (i.e., highly repulsive locally but sufficiently thin to keep small interparticle gap).[31] Recently, Yao et al. employed polyvinylpyrrolidone (PVP) to facilitate the self-assembly of 45 nm Au NPs into monolayers at the air/water interface.[38] Because of large interparticle spacing, these monolayers are not of interest for SERS. The aforementioned approaches rely on concentration or chemistry to stabilize large Au NPs, which limits the ability to control NP surface coverage and chemistry.

We have developed a technique that can functionalize 13 nm Au NPs with ligands ranging from small molecules to polymers and assemble them into monolayers.[39] It uses sequential migration from a liquid–liquid interface, where ligand attachment occurs, to a liquid–air interface, where assembly occurs. The NP surface coverage is controlled by the residence time at the liquid–liquid interface, which gives greater flexibility in tuning the concentration of ligand. The spontaneous translocation of Au NPs from water/organic interface to water/air interface is a result of the minimization of the Helmholtz free energy, which is NP size-insensitive. Herein, we demonstrate

DOI: 10.1021/acsami.7b01121
ACS Appl. Mater. Interfaces 2017, 9, 13457–13470

that the three-phase self-assembly technique can be extended to regulate large Au NPs up to 92 nm to form Au NP monolayers. The monolayers have a long-range ordering, with a local hexagonally close-packed (HCP) structure. We further demonstrate that the optimized Au NP arrays exhibit SERS enhancement factors (EFs) up to 10^7 for the model analyte rhodamine (R6G) and high performance battery electrolytes such as lithium bis(trifluoromethane)sulfonimide salt (LiTFSI).

RESULTS AND DISCUSSION

Au NP Size Distribution. TEM images in the upper panel of Figure 1 indicate that the as-synthesized Au NPs using seed-growth method are for the most part spherical. Statistical analysis of the TEM images shows that all Au NP samples have low size dispersity (less than 8%) with a Gaussian distribution. The average particle diameters, D, are listed in Table 1.

Au NP Monolayer Self-Assembly. As shown in Scheme 1a, a triphase system composed of water, oil, and air was used to assemble Au NPs into monolayers.[39] Ethanol was added to the system, increasing the particle/water surface tension, $\gamma_{P/W}$,[40] decreasing NP surface charge, and driving the Au NPs to the water/oil interface (Scheme 1a, step I). At the water/oil interface, alkylamine ligands replace ethanol and residual negative charge on the Au NP surface.[12,22] This allows self-assembly to begin in the form of small islands. The Au NP islands rapidly move to the water/air interface where they coalesce into a monolayer (Scheme 1a, step II). This monolayer was then deposited on solid substrates by removing the water.[20]

The three-phase system is theoretically insensitive to NP size. In this study, we experimentally test this prediction. Shown in Scheme 1b, it has been proposed by similar studies that a NP will remain at a liquid/liquid interface if the contact angle between the particle and the interface is 90°, i.e., $\gamma_{P/W} = \gamma_{P/O}$.[41,42] Thus, the interfacial energy change due to the translocation of a NP from the water phase to the oil/water interface can be written as[43]

$$\Delta E_{O/W} = -\pi r^2 \gamma_{O/W} \quad (1)$$

Recognizing that a dense NP under the force of gravity cannot fully reside in air, the condition for it to remain at a water/air interface is $\gamma_{P/A} \geq \gamma_{P/W}$. Thus, the interfacial energy change for a NP moving from water to a water/air interface is[39]

$$\Delta E_{W/A} \leq -\pi r^2 \gamma_{W/A} \quad (2)$$

The minimum free energy difference (ΔE_{drive}) to drive a NP from the oil/water interface to the water/air interface is the difference of eqs 1 and 2.

$$\Delta E_{drive} = \Delta E_{W/A} - \Delta E_{O/W} \leq -\pi r^2(\gamma_{W/A} - \gamma_{O/W}) \quad (3)$$

The water/air surface tension is $\gamma_{W/A}$ = 71.9 mJ m^{-2},[44] and the interfacial tension between the oil phase and water is $\gamma_{O/W}$ = 50.7 mJ m^{-2}.[39] Therefore, the driving force for Au NPs to move from the oil/water interface to the water/air interface is $\Delta E_{drive} \leq -21.2$ (mJ m^{-2})·πr^2. Since $r > 0$, ΔE_{drive} is negative for all NP sizes, indicating that a NP will spontaneously move from the oil/water interface to the water/air interface regardless of size. However, the magnitude of the driving force, ΔE_{drive}, depends on the square of NP radius. Consequently, ΔE_{drive} increases rapidly from that for S13Au to that for S90Au (Table 2). It is worth noting that for each Au NP size $\Delta E_{W/A}$ is orders of magnitude greater than the thermal fluctuation energy, which is the driving force for detaching a NP from an interface.[42] So, once assembled at the water/air interface, the monolayers are stable until deposition.

Scheme 1. (a) Protocol of Self-Assembling Aqueous Au NPs into a 2D Monolayer;[a] (b) Qualitative Interfacial Free Energy Diagram for a Single Au NP at Water Phase ($E_{P/W}$), Oil Phase ($E_{P/O}$), and Air Phase ($E_{P/A}$)[b]

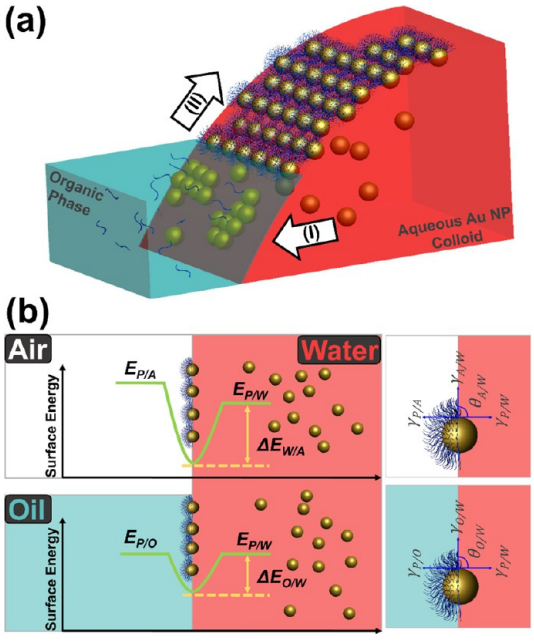

[a](I) upon ethanol addition, the Au NPs relocate from water phase to the water/oil interface, where the alkylamine ligands attach to the Au NP surface. (II) The Au NPs spontaneously move to the water/air interface from the water/oil interphase to form a monolayer there. [b]When at two-phase interfacial area, the Au NP has a lower surface free energy than that when NPs are dispersed in a single phase. However, the decrease of the total free energy for an Au NP at the water/air interface is larger than that at the oil/water interface (i.e., $\Delta E_{W/A} > \Delta E_{O/W}$). Thus, the free energy difference is capable of driving Au NPs from the oil/water interface to the water/air interface. We denote the phase in contact with water as "α" (α is either oil or air). The interfacial energy originates from three contributions, namely, the particle–α surface tension, $\gamma_{p/\alpha}$, the particle–water surface tension, $\gamma_{p/W}$, and the α–water surface tension, $\gamma_{\alpha/W}$. "$\theta_{\alpha/W}$" Represents the contact angle between the particle and the α/W interface and is related to the three contributions of the interfacial energy by Young's equation,[42] $\cos\theta_{\alpha/W} = (\gamma_{p/\alpha} - \gamma_{p/W})/\gamma_{\alpha/W}$.

Table 2. Driving Force, ΔE_{drive}, To Relocate NPs from the Water/Oil Interface to the Water/Air Interface of Each Au NP Monolayer

sample ID	ΔE_{drive} (mJ)	$\Delta E_{drive}/k_bT$[a]
S13Au	2.69×10^{-15}	6.53×10^2
S40Au	2.25×10^{-14}	5.47×10^3
S60Au	5.21×10^{-14}	1.27×10^4
S90Au	1.40×10^{-13}	3.40×10^4

[a]Boltzmann constant $k_b = 1.38 \times 10^{-20}$ mJ K^{-1} and with temperature T = 298 K.

Au NP Monolayer Characterization. The SEM micrographs in Figure 2a demonstrate that each of the four sizes of Au NP was successfully assembled into monolayers using the three-phase method, in agreement with the theoretical

DOI: 10.1021/acsami.7b01121
ACS Appl. Mater. Interfaces 2017, 9, 13457–13470

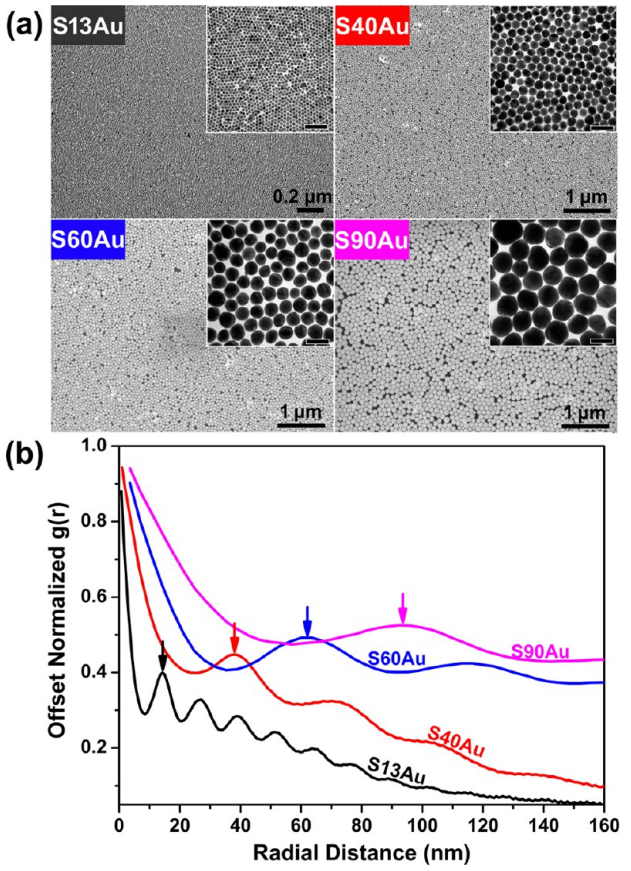

Figure 2. (a) SEM and TEM (inset) images of various Au NP monolayers deposited on silicon wafers and carbon-coated TEM copper grids. The scale bar is 100 nm for all TEM images. (b) Plot of normalized radial distribution as a function of the radial distance for each Au NP monolayer. The arrow indicates the primary peak, with the *x*-axis value corresponding to the average center-to-center distance, $d_{c\text{-}c}$, of each Au NP monolayer.

prediction.[39] The monolayers were of decent order across a significant area. There appears to be a minor but noticeable increase in defect density with increasing NP size. This could be due to either ΔE_{drive} increasing with increasing NP size or to mobility decreasing with increasing NP size. Lower mobility would limit the ability for defects to be removed via NP rearrangement at the water/air interface. SEM images (Figure S1) of lower magnification show that the Au NP monolayers maintain order over areas up to 300 μm^2, which is at least 1 order of magnitude higher than that which is required for making uniform NP-based SERS wafers.[13] TEM images (Figure 2a, inset) of higher magnifications indicate that the Au NP films have a local HCP structure. The lack of overlapping features also demonstrates that the films are a single layer. The order of the Au NP films in Figure 2a is in sharp contrast to the structure of drop-cast NPs, as shown in the upper panels of Figure 1. The three-phase self-assembly technique does not exhibit an obvious Au NP size selection effect. In fact, the NP size distribution after the self-assembly process (Table S3) is not statistically different from that of the aqueous colloid. This is in agreement with eq 3 that predicts a size insensitivity for the three-phase self-assembly method. To further evaluate this point, we assembled an NP monolayer using an equivolume mixture of S13Au and S90Au NPs. The Au NPs of both sizes assembled together are shown in the TEM micrograph of Figure S2.

The center-to-center distance ($d_{c\text{-}c}$) of the NPs was quantified by statistically analyzing TEM micrographs. The result of this analysis is the radial distribution function, $g(r)$, which is shown in Figure 2b for monolayers of each NP size.[20] At least three monolayers were analyzed for each NP size. The primary peak of $g(r)$, indicated by an arrow in Figure 2b, represents $d_{c\text{-}c}$ and is reported in Table 1. $d_{c\text{-}c}$ increases from S13Au film to S90Au film, which is due to the increased average NP diameter. The interparticle gap, d_{gap}, can then be calculated by $d_{gap} = d_{c\text{-}c} - D$.[20] The d_{gap} values of S13Au and S60Au are approximately twice those of S40Au and S90Au. The full width at half-maximum of the primary $g(r)$ peak normalized to D is also larger for S13Au and S60Au than for S40Au and S90Au. We suspect this is related to the slightly larger maximum areal ligand densities used in preparing S13Au and S60Au films (see Methods section for details). The gap between particles is filled with ligand. Therefore, excess ligand can swell d_{gap} and increase the distribution of gap sizes.

The local field enhancement increases strongly as the dimensionless ratio, D/d_{gap}, increases for Au NP monolayers.[45] This ratio is reported in Table 1. It is smallest for S13Au and largest for S90Au, indicating that the absolute magnitude of D plays a dominant role when fixed ligand length is used. We have shown in previous work that d_{gap} can be controlled by ligand length.[12] S40Au has a larger D/d_{gap} ratio than S60Au due to S60Au having a larger d_{gap} than S40Au. This is due to S40Au having the lowest maximum areal ligand density and S60Au monolayers containing more defects than S40Au monolayers.

AFM was used to validate the TEM analysis of the structure and dimensions of the Au NP films. The 3D AFM reconstruction of each Au NP film is shown in Figure 3. Measurements were taken near the edge of each Au NP film, so that the height profile between the top of the NP film and the Si wafer could be extracted. For each Au NP film, the center-to-center distance, $d_{c\text{-}c}$, was calculated from a line profile along the dashed line in each 3D reconstruction. Line profiles are shown below the corresponding 3D reconstruction in Figure 3. The average wavelength of the line profile, λ_d, is equal to the center-to-center distance, $d_{c\text{-}c}$, of each film. The value of λ_d was calculated by dividing a known distance, L, by the number of periods, n, in the line profile. The average height and wavelength values obtained from AFM images for each Au NP film are included in Table 1. It is worth noting that the average height, h, is slightly larger than the corresponding Au NP diameter, D, possibly because the AFM tip scans the top of the outer ligand shell of each NP. The difference between the AFM height, h, and the average diameter, D, is from 3 to 5 nm for different Au NP films, which corresponds to one or two C18-NH_2 alkyl chain lengths.[12] As shown in Table 1, the wavelengths, λ_d, obtained from AFM agree reasonably well with $d_{c\text{-}c}$ from TEM.

Au NP LSPR Analysis. As reported by Nordlander et al.,[46] the plasmons of complex NP assemblies can be treated as a hybridization of individual nanoparticle plasmons. Thus, it is of interest to perform detailed analysis of the LSPR bands of individual nanoparticles before examining monolayer assemblies. Individual Au NP LSPR was measured using UV−vis spectroscopy on dilute aqueous Au NP dispersions. The spectrum from each Au NP size is shown in Figure 4. In agreement with many other literature reports, the SPR maximum red-shifts with increasing the NP size.[47] Also

DOI: 10.1021/acsami.7b01121
ACS Appl. Mater. Interfaces 2017, 9, 13457−13470

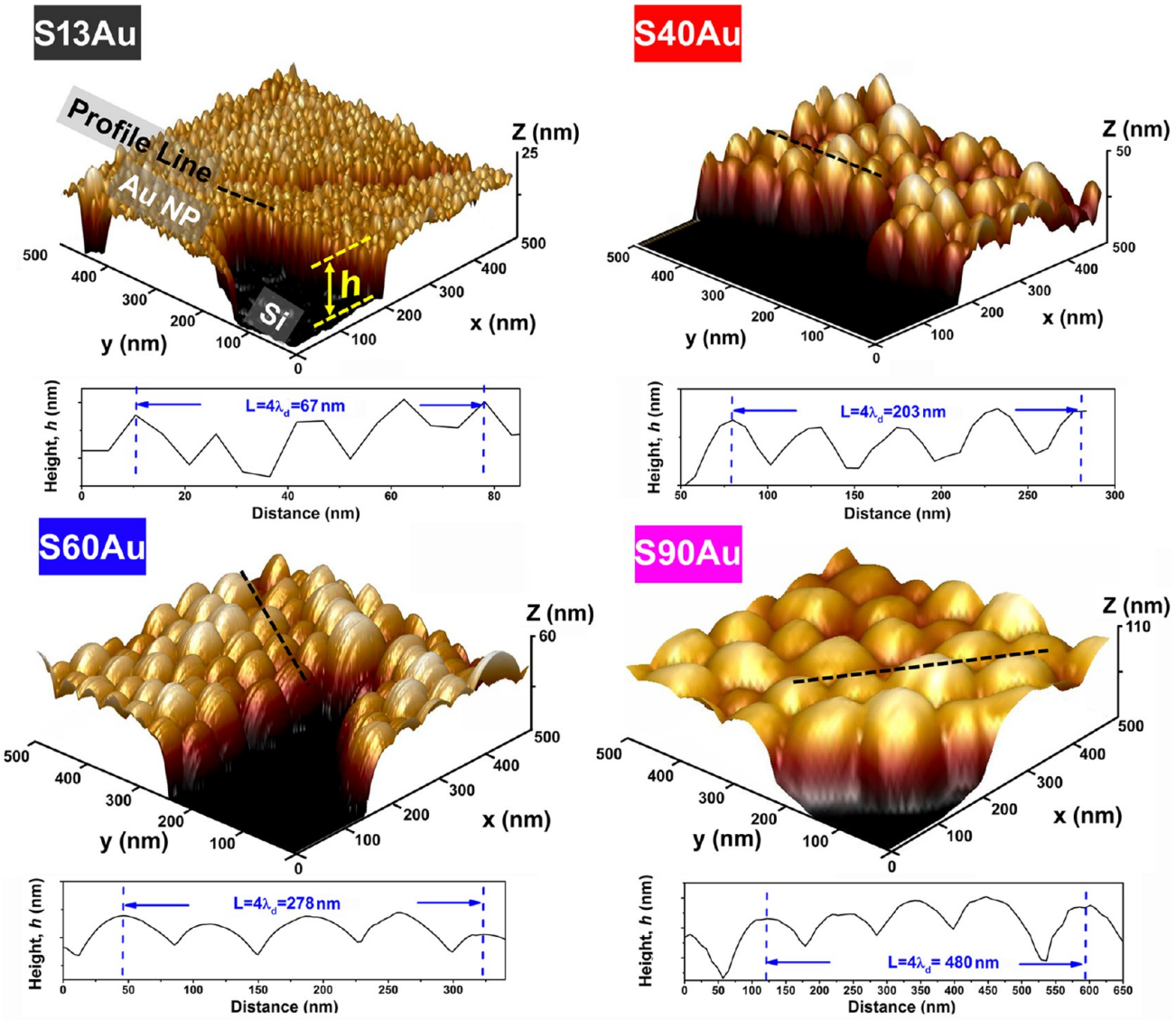

Figure 3. Upper panels: 3D AFM reconstruction of each Au NP monolayer taken near film edge. Lower panels: 1D AFM height profile taken along the dashed line in each 3D AFM reconstruction. The value of L corresponds to four wavelengths of the horizontal AFM line profile of each sample.

shown in Figure 4 are simulated extinction spectra for each Au NP size. Loss of electromagnetic energy due to light interacting with matter (i.e., extinction) results from two contributions: scattering and absorption.[48,49] Each of these contributions was calculated separately using FDTD simulations and is also reported in Figure 4. For each Au NP size, the simulation results are reported as a dimensionless Mie efficiency that is obtained by dividing the optical cross section by the physical cross-sectional area (i.e., πR^2). It is worth noting that the total extinction efficiency increases with the increasing NP size, from 0.8 for S13Au to 6.5 for S90Au. It is also apparent that the absorption and scattering efficiencies are strongly dependent on NP size. For S13Au, the extinction efficiency is almost completely dominated by absorption. As the NP size becomes larger, the portion contributed by scattering increases dramatically as expected. For S90Au, absorption and scattering contribute to extinction almost equally. From Figure 4 (also see Table S3), our simulated results agree reasonably well with the experimental results. Our results are in close agreement with calculations reported earlier by El-Sayed et al. using full Mie theory.[50] They found that nearly all the contribution to extinction was from absorption for Au NPs smaller than 20 nm. Above the threshold of 40 nm, the scattering to absorption ratio started to increase.

The LSPR of each Au NP monolayer was studied by UV−vis−NIR spectroscopy. The results are shown in Figure 5. Unlike the isolated Au NPs whose LSPR peaks are limited to the visible light region, the Au NP monolayers have LSPR absorbance that extends into the NIR. According to Mie theory,[51] the LSPR extinction efficiency depends on the particle size, shape, composition, and the dielectric constant of the surrounding medium. A significant LSPR band red-shift was observed for the Au NP monolayer deposited on the glass slides compared to its Au NP colloidal counterpart. When two NPs are brought close to each other, the near-field of one NP interacts with that of its neighbor, coupling the plasmon oscillations.[52] The coupled SPR mode is known to be determined by the interparticle gap, d_{gap};[47,53] i.e., the smaller the interparticle gap, the stronger the interparticle coupling and hence the larger is the SPR band red-shift.[12] Thus, the SPR maximum position and the bandwidth can be ascribed to the synergetic effects of the single NP plasmon oscillation and the

DOI: 10.1021/acsami.7b01121
ACS Appl. Mater. Interfaces 2017, 9, 13457−13470

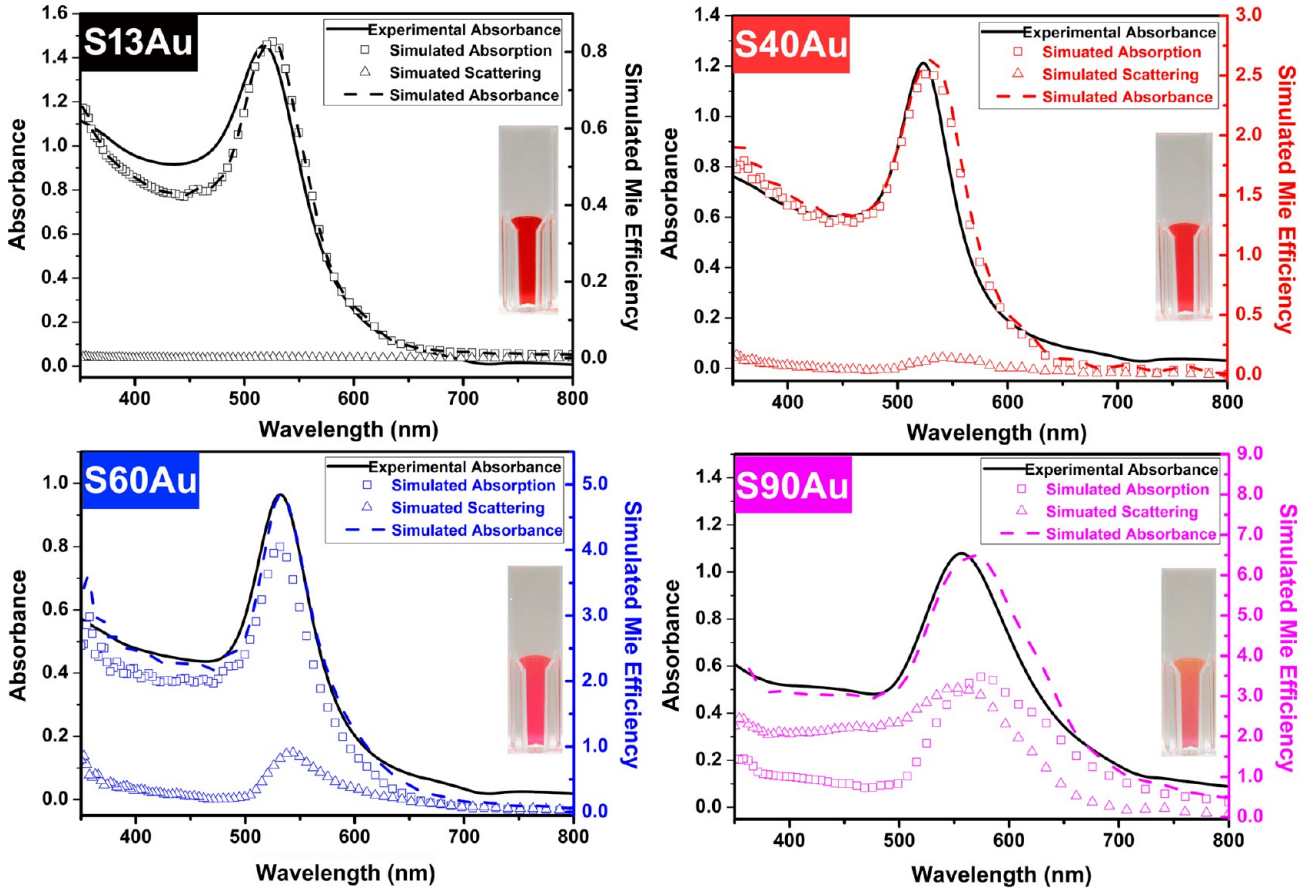

Figure 4. Comparison of the experimental UV−vis absorbance and FDTD simulated absorbance efficiency for each Au NP colloid. The simulated absorbance efficiency is contributed by absorption (squares) and scattering (triangles). The inset is a photograph of 1 mL of each Au NP colloid in a transparent polystyrene cuvette. The color of aqueous Au colloids is due to the sum of the effects of visible light absorption and scattering.[81]

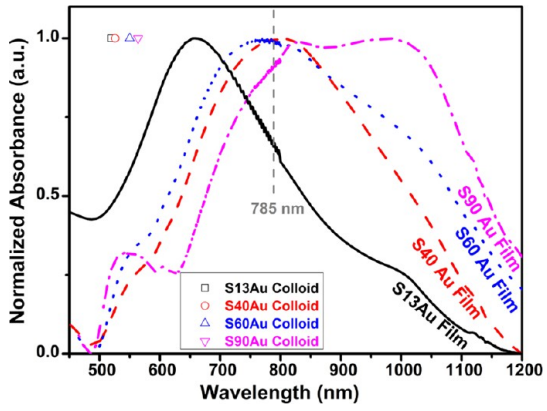

Figure 5. UV−vis−NIR absorption spectra of different Au NP monolayers deposited on glass slides. For reference, the SPR maximum of the corresponding Au NPs dispersed in water are shown as data points. The gray dashed line represents the Raman laser wavelength at 785 nm. Each spectrum is normalized by its absorbance maximum.

plasmon coupling oscillation.[54] We use the NP diameter to interparticle gap (D/d_{gap}) ratio to better quantify this point. For reference, the LSPR maximum of the 40 nm aqueous colloid is 24 nm smaller than that of the 60 nm aqueous colloid at 550 nm. However, the S40Au film has a slightly larger wavelength LSPR than that of the S60Au film (Table S3). This is due to S40Au having a larger D/d_{gap} ratio. In this work, we have focused on the LSPR properties of neat Au NP monolayers, but we note that the presence of analyte can modify the local dielectric constant and affect the LSPR. In future work, we will investigate such effects with analytes that do not fluoresce.

It is also worth noting that there are secondary peaks in the UV−vis−NIR spectrum of each monolayer. Details of peak location determination are described in the Supporting Information. Taking S90Au as an example, secondary peaks occur at 560, 608, 824, and 1031 nm. The contribution of multipolar resonances to total scattering has been shown to increase with increasing particle size.[55−57] In accordance with this literature, we attribute these secondary peaks to higher order multipolar resonances.

Au NP Monolayer SERS Properties. Analytical molecular detection with SERS is quite promising for sensitive measurements of adsorbed and nearby molecules. Therefore, we further investigated the potential of Au NP monolayers for SERS applications. Rhodamine 6G (R6G) was used as a model Raman analyte to evaluate the SERS performance of the Au NP monolayers. A laser wavelength of 785 nm was used to achieve good Raman signal while minimizing background fluorescence. This wavelength is in close proximity to or within the major SPR bands of the S40Au film, S60Au film, and S90Au film (Figure 5). One would expect a shorter wavelength laser to be optimal for S13Au film, but background fluorescence became problematic when we attempted to use a 638 nm laser. Raman spectra of R6G on each of the Au NP films are shown in Figure 6a. Numerous bands are apparent. Also shown in Figure 6a is

DOI: 10.1021/acsami.7b01121
ACS Appl. Mater. Interfaces 2017, 9, 13457−13470

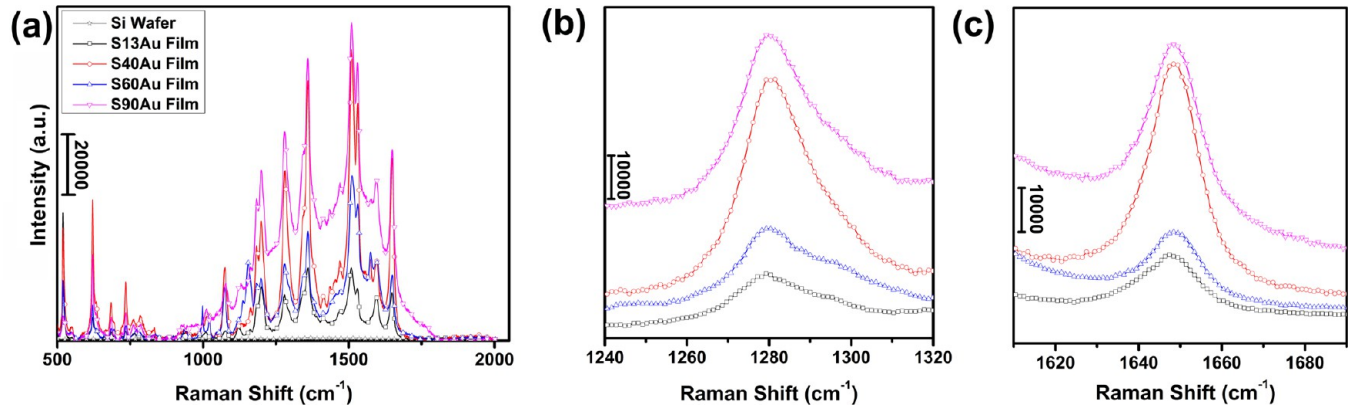

Figure 6. (a) SERS spectrum of R6G dried from ethanol solution (1 μL, 1 mM) on various Au NP monolayers. For contrast, normal Raman spectrum was collected from R6G on silicon substrate as a reference. The more detailed SERS spectra of (b) C−O−C stretching (ν_{C-O-C}) and (c) aromatic C−C stretching (ν_{C-C}) for R6G.

the Raman spectrum of R6G on a bare silicon wafer. In contrast, no Raman bands can be seen at this scale without the enhancement of the Au NP monolayers. The Raman signal without surface enhancement is orders of magnitude lower than with enhancement due to the low cross section of the normal Raman scattering.[58] This indicates that the Au NP monolayers used in this study have promising SERS activity, with S40Au film and S90Au film showing the strongest intensity for most R6G Raman bands. It is noteworthy that a large background signal was observed with the S90Au film. This is most likely due to significant fluorescence enhancement by secondary LSPR peaks of S90Au at short wavelength.[59] The Raman scattering enhancement factor (EF) of the Au NP monolayers was calculated by[20]

$$\mathrm{EF} = \left(\frac{I_{\mathrm{SERS}}}{I_{\mathrm{o}}}\right)^2 \tag{4}$$

I_{SERS} is the peak integration of the enhanced Raman band, and I_{o} is the integration of the corresponding normal Raman band on silicon. Since the laser is incident normal to the film surface, detection occurs in backscatter configuration, and R6G has uniaxial Raman tensors;[60] eq 4 is a good approximation for the magnitude of SERS enhancement.[61] In fact, we have found eq 4 to slightly underpredict EF as compared to explicitly accounting for the number of molecules involved in normal Raman scattering and those detected by SERS. We prefer the simplicity of eq 4 because it allows us to subtract background fluorescence contribution to the Raman signal. For R6G we used the C−O−C stretching band at 1280 cm^{-1} (Figure 6b) and the aromatic C−C stretching band at 1650 cm^{-1} (Figure 6c) to perform the EF calculation. The average R6G areal density on the substrate was estimated to be 1×10^{-10} mol/mm^2 based on the R6G/ethanol droplet volume, concentration, and contact area with the substrate (7 mm^2). The EF of S40Au film is 6.2×10^7 for C−O−C stretching and 3.6×10^7 for that of the S90Au film. These values are an order of magnitude larger than those for S13Au at 3×10^6 and for S60Au at 6×10^6. For all Au NP monolayers, there are slight differences between EFs calculated from different vibrations. This is to be expected because the surface enhancement is due to not only LSPR enhancement of incident radiation but also enhancement of Raman scattered radiation.[11] The LSPR of S40Au film is located at shorter wavelength but close to the incident laser wavelength (see Figure 5). Therefore, the enhancement of Raman scattering is expected to be greater for peaks with smaller Raman shift, which is the case. Another consideration when Raman band-dependent EF is observed is the proximity and orientation of each molecular bond with respect to the hot spots.[62] On the basis of these findings, we cannot comment on this contribution.

Besides large Raman scattering enhancement, other requirements for a reliable SERS substrate include good spatial homogeneity, long shelf life, and ability to quantify analyte concentration.[63] We use the S40Au NP monolayer to demonstrate the spatial homogeneity of the Raman intensity. As shown in Figure 7a, SERS spectra of R6G were collected from 105 different locations. The inset of Figure 7a shows a histogram of the 1650 cm^{-1} (aromatic C−C stretching) integration at each location. A small relative standard deviation (RSD = 3.1%) demonstrates the homogeneous SERS response across the length scale of 1.2 mm on the Au NP monolayer. The total size of the Au NP monolayer is on the order of 10 mm^2, which is sufficient for applications such as analyte detection. There are no inherent limitations to scaling up the three-phase assembly method which is limited only by the quantity of Au NP colloid and the substrate dimensions.

The shelf life of our monolayers was evaluated by examining the SERS performance of the S40Au film after 8 months storage at room temperature. The R6G SERS spectrum on the stored film compared to that on a freshly deposited S40Au monolayer is shown in Figure 7b. Although the peak integration at 1280 cm^{-1} band (inset of Figure 7b) shows a small decrease (18% ± 2%) in SERS activity after 8 months, the Raman bands of the R6G were still clearly apparent.

We evaluated the quantitative accuracy of the Au NP monolayers as SERS substrates by using different concentrations of R6G. In order to do so, 1 μL of R6G ethanol droplets ranging from 50 nM to 1 mM were placed on the S40Au films and dried. As shown in the log−log plot of Figure 7c, the integrated C−O−C stretching band intensity at 1280 cm^{-1} increases in a power law fashion (power = 0.4) with R6G concentration, which is in good agreement with our previous study[20] and those of others.[64] It is worth noting that the lowest R6G concentration detection limit for S40Au monolayer is 10^{-8} M, 3 orders of magnitude lower than that detectable by the 13 nm Au NP film in our previous report.[20] The detection limit for the large Au NP monolayer fabricated using the triphase method is also comparable with 2D ensembles of gold nanorods self-assembled at a liquid−liquid interface.[65] The

DOI: 10.1021/acsami.7b01121
ACS Appl. Mater. Interfaces 2017, 9, 13457−13470

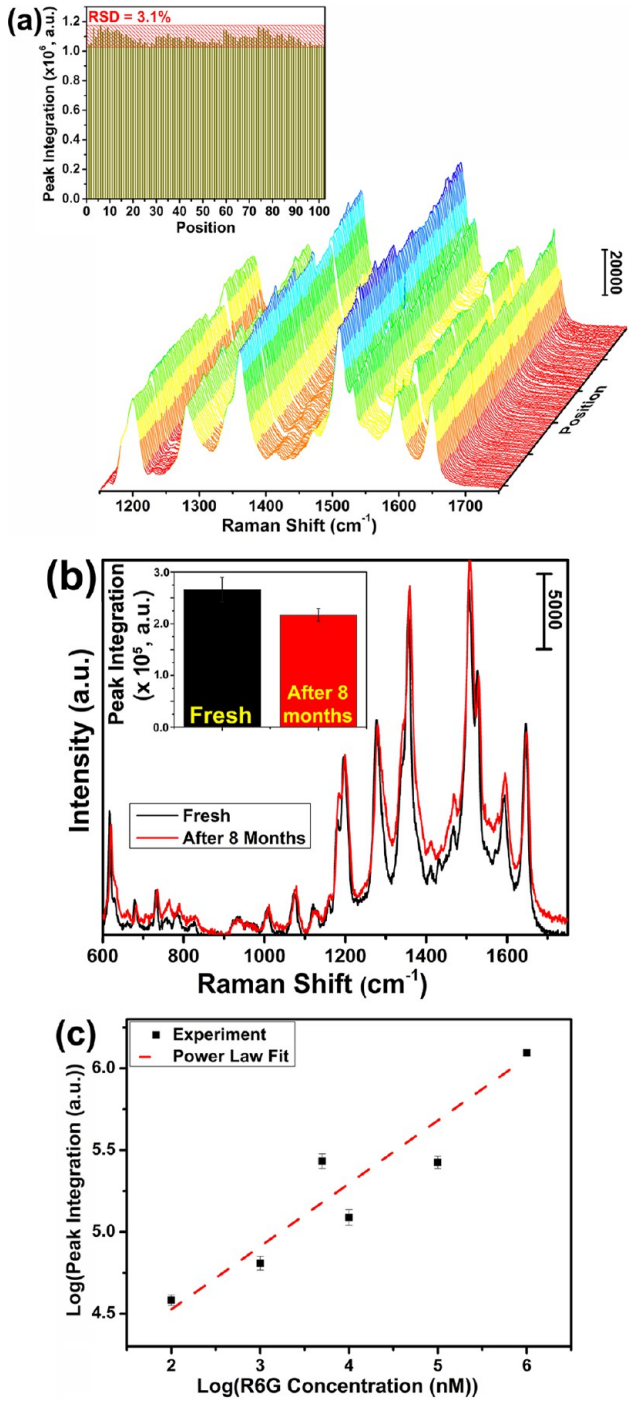

Figure 7. (a) Spatial homogeneity demonstration of the SERS performance using the S40Au monolayer. The SERS spectra were collected from seven different positions at least 200 μm apart from each other. The spectra were collected from 15 locations (point-to-point distance = 4 μm) in a rectangular frame from each position. Inset is the integrated intensity of the R6G aromatic C−C stretching band from 1620 to 1750 cm^{-1}. (b) Long-term SERS stability demonstration using the S40Au monolayer. The SERS spectra of R6G (0.1 mM ethanol solution dried on Au monolayer) were taken from a freshly deposited S40Au film (black line) and from an S40Au film after 8 months (red line). Inset shows the peak integrated C−O−C band at 1280 cm^{-1} for both samples. The error bar stands for the standard deviation of three measurements of three locations randomly chosen from each sample. (c) The log−log plot of the C−O−C stretching band integration versus the R6G/ethanol solution concentration and its power law calibration curve.

Au NP monolayers assembled using three-phase method are promising for quantitatively detection of trace amount of analytes on *solid* substrates.

The last SERS property we tested on the 40 nm Au NP monolayers is their versatility in enhancing the Raman scattering from other analytes, such as LiTFSI used in polymer electrolytes for lithium batteries. LiTFSI was dissolved in *N*-methyl-2-pyrrolidone (NMP) at 0.1 mM. Shown in Figure 8a, the SERS spectra of LiTFSI/NMP solution collected from different Au NP monolayers exhibit several prominent Raman bands that can be attributed to $TFSI^-$ and NMP. The SERS bands between 555 and 715 cm^{-1} are attributed to the molecular bond vibrations related to sulfur in $TFSI^-$. For example, the band at 618 cm^{-1} represents the out-of-plane O−S−O asymmetric bending (δ_{aSO_2}).[66] The bands between 857 and 987 cm^{-1} can be assigned to the ring modes of NMP.[67] The peak at 1303 cm^{-1} is attributed to NMP $-CH_2$ twisting (τ_{CH_2}),[68] and the small group of peaks between 2849 and 2985 cm^{-1} is attributed to $-CH_2$ stretching in NMP. Peak assignment details can be found in Table S5. The EFs were quantified using δ_{aSO_2} of $TFSI^-$ (Figure 8b) and τ_{CH_2} of NMP (Figure 8c).

The EFs of all analytes examined in this study are shown in Figure 8d as a function of the D/d_{gap} ratio. For LiTFSI and NMP the EFs calculated for S13Au, S60Au, and S90Au are smaller than 10^5, whereas the EF for S40Au reaches 10^6. The SERS EFs of LiTFSI/NMP solution are 1−3 orders of magnitude lower than those of solid R6G. This can be attributed to the specific affinity of R6G for gold.[69] The molecular orientational averaging of the liquid analyte molecules may also contribute to lower Raman intensity.[62] We also notice from Figure 8b,c that the same analytes exhibit slightly different Raman bands at the same Raman shift region on different Au NP monolayers. This might be explained by the Raman noncoincidence effect.[70] More specifically, the geometry of the interparticle gap is different among Au NP monolayers, possibly resulting in different preferred orientations of NMP molecules and solvated $TFSI^-$ anions versus the hot spot of various NP films. Thus, the isotropic and anisotropic Raman components of each species appear at different positions. In any case, the Raman signal of this lithium salt at low concentration demonstrates the feasibility of using our robust Au NP monolayers as SERS substrates for studying lithium batteries. We anticipate this approach being of particular interest for investigating the solid electrolyte interphase that forms between battery electrodes and electrolyte.

FDTD Simulation and Analytical Calculation. To investigate the hot spot distribution on various NP monolayers, we performed 3D FDTD simulations by numerically solving Maxwell's equations.[39] In this work we report the distribution of enhancement factors eq 4 across HCP films of each NP size. The simulation results are shown in Figure 9a. The maximum simulated EF order increased from 10^5 for S13Au NP monolayer to 10^8 for S40Au film and S60Au film and to 10^9 for S90Au film. The orders of magnitude increase in EFs for large Au NP monolayers clearly demonstrates that they are promising candidates for sensitive SERS substrates. It is also apparent from the simulated EF maps that complex LSPR coupling occurs among the collection of NPs. The nanoparticle dimer is the simplest but important prototypical coupling system for studying the EM field enhancement, and the dimer plasmons can be considered as the combination of the

DOI: 10.1021/acsami.7b01121
ACS Appl. Mater. Interfaces 2017, 9, 13457−13470

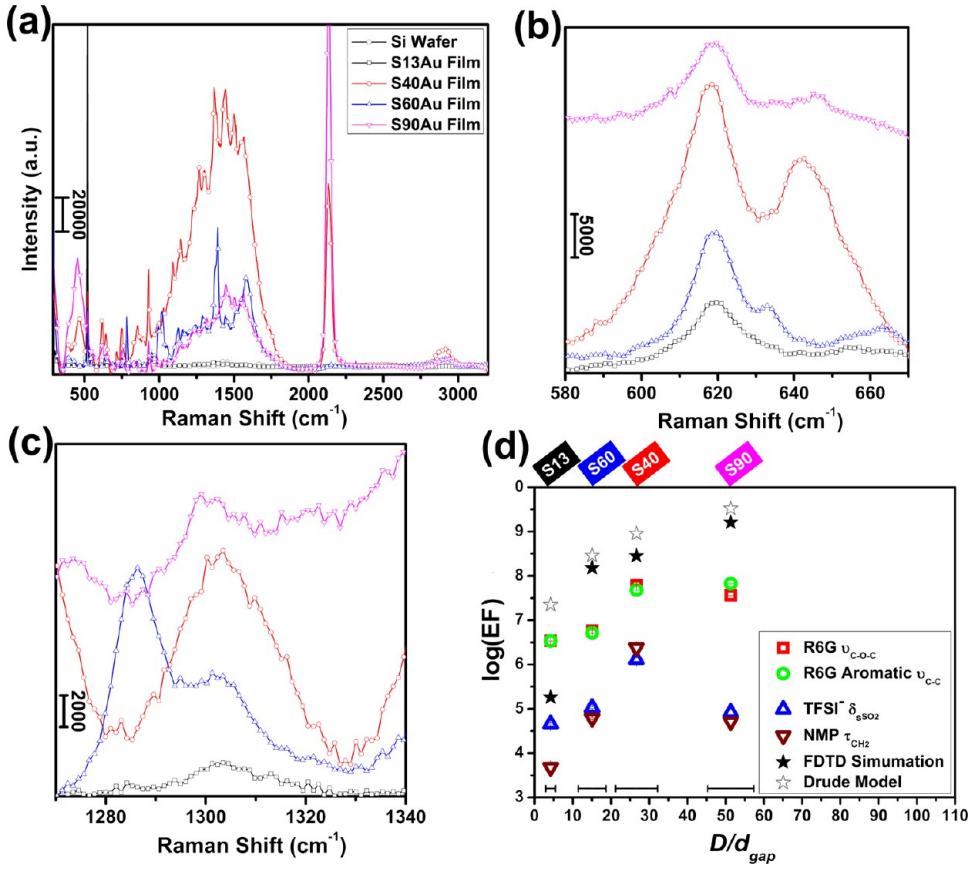

Figure 8. (a) SERS spectra of LiTFSI in NMP (0.1 mM) on various Au NP films. The normal Raman spectrum was taken from LiTFSI/NMP (0.1 mM) on silicon wafer. More detailed SERS spectra of (b) symmetric SO_2 bending (δ_{sSO_2}) for $TFSI^-$ and (c) CH_2 twisting (τ_{CH_2}) for NMP measured from various Au NP monolayers. (d) A comparison among the EFs collected from experiments on various chemical bands, the FDTD simulated results, and the calculated results using the Drude model as a function of diameter/gap ratio. The error bar is calculated based on the error propagation related to the NP diameter and the interparticle gap.

individual NP plasmonic dipole moments.[46] And if the polarization direction of the incident light is parallel to the NP center-to-center axis (interparticle axis), the hot spot of the maximum EF is usually found on the interparticle axis at the NP surface.[71] However, the EM-field spatial distribution on an HCP NP matrix is intrinsically more complicated than that of a NP dimer due to the overlap of the dipolar and multipolar plasmon modes.[72] Thus, it is of interest to study the spatial distribution of the EF in more detail for these Au NP monolayers. As shown in Figure 9a, lower panel, the orders of EFs in the vicinity of a reference NP are marked by arrows. For all Au NP films, the maximum EF is not along the interparticle axis. This may be because the polarization direction of the incident light was not parallel to the interparticle axis. To further quantify the spatial distribution of the maximum EF value for each Au NP monolayer, we studied the distance between the hot spot and the reference NP surface, d_{hs}, and the angle, θ_h, between the NP center-to-hot spot line and the interparticle axis (see Figure 9b schematic). In Figure 9a, white dashed lines intersect a maximum EF (hot spot) near a reference NP. The 1D EF profiles along these lines are shown in Figure 9b. The surface of the reference NP is denoted by a short, vertical, gray dashed line in Figure 9b. The hot spot was found to be close to the reference NP surface for all samples. The small values of d_{hs} for all Au NP monolayers further validate the near-field enhancement mechanism for all Au NP monolayers.[12] θ_h is also reported in Figure 9b. It is smallest for the S40Au film (1.68°) and an order of magnitude higher for the other three Au NP monolayers. The value of θ_h appears to be dependent on the polarization vector, *E*, constituent Au NP size, and interparticle spacing. More detailed FDTD study on the polarization angle effect on the SERS of various Au NP films is ongoing.

In addition to the location of maximum EFs, we observe regions where the EF is less than one. This means that the local EM intensity is less than the incident EM intensity. A black dotted line intersects these EF minima in Figure 9a, lower panel. The 1D EF profiles along these lines is shown in Figure 9c, and the interparticle axes are denoted by vertical dashed lines. These regions of destructive plasmon interference occur where the interparticle axis is orthogonal to the polarization vector, *E*. We attribute this phenomenon to the destructive interference of induced electron oscillations among adjacent Au NPs in the HCP unit cell. For nanocube dimers, there is one recent report of cold spots,[73] but we are not aware of any reports of cold spots in NP assemblies.

The decreased interparticle gap between Au NP dimers resulted in a stronger EM coupling and hence a larger EM field in the vicinity of the gap.[74] In addition, the constituent NP size cannot be ruled out from contributing to the enhanced EM. It has been found that with the NP size increase, the retardation effects becomes more important,[75] and the NP polarizability increases modestly.[76] This in turn affects the enhanced EM field across the Au NP monolayers with a certain incident light

DOI: 10.1021/acsami.7b01121
ACS Appl. Mater. Interfaces 2017, 9, 13457−13470

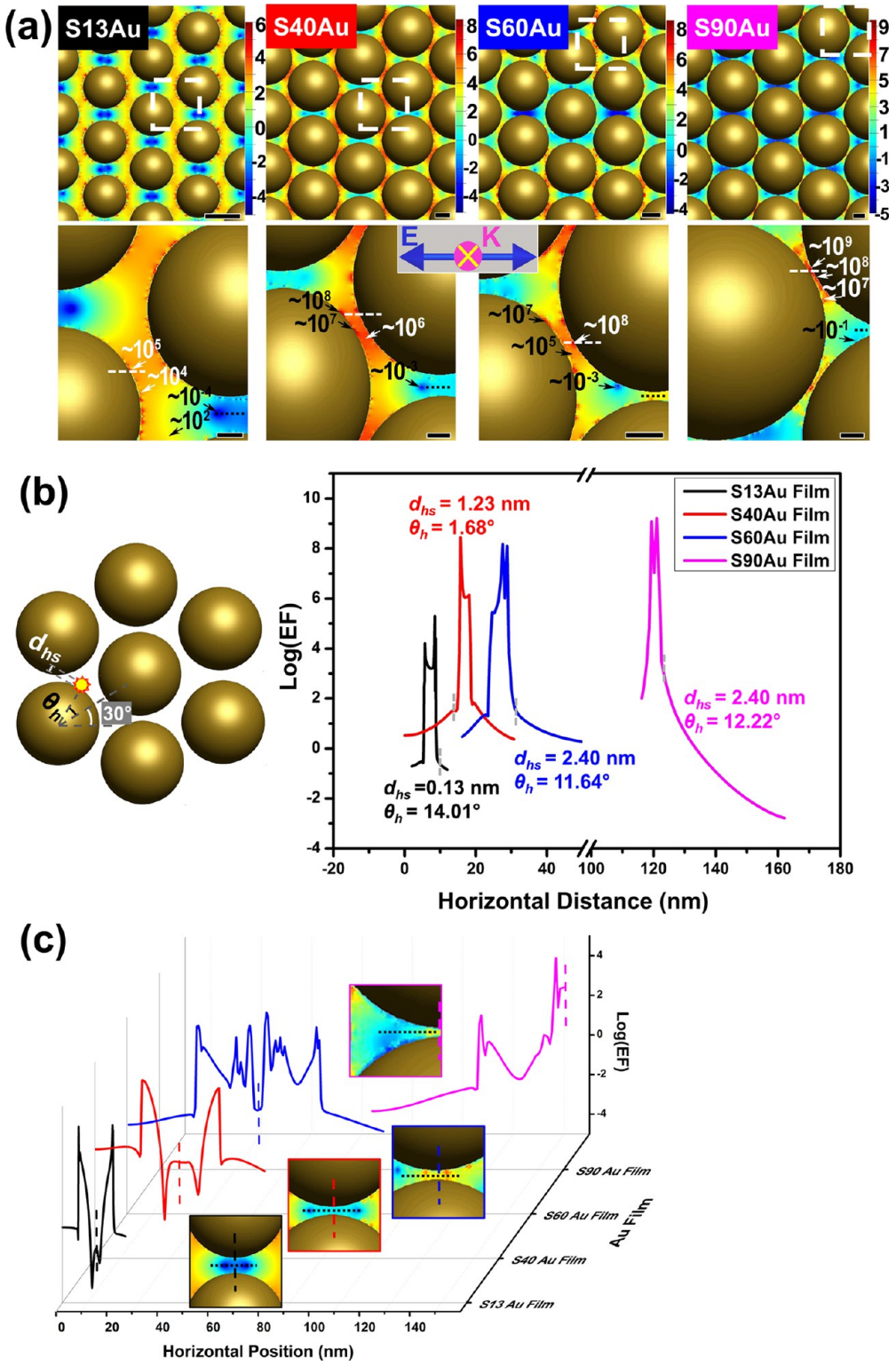

Figure 9. (a) 3D FDTD simulation of various Au NP monolayers deposited on silicon wafer. In the center gray box, the blue arrow represents the polarization direction of the electric field (*E*-field), **E**, at 785 nm, whereas the pink arrow, **K**, indicates that the *E*-field propagates perpendicular to the plane of paper inside. Each bottom image corresponds to the area included by the white dashed box in the top image. The color bar represents the log(EF) of each sample. Single arrows indicate local EFs. The horizontal white dashed line cuts the max EF for each of the Au NP film, and the black dotted line horizontally cuts the interparticle space center. The scale bar is 10 nm for S13Au and S40Au and 20 nm for S60Au and S90Au for top images and is 2 nm for S13Au, 4 nm for S40 Au, and 10 nm for S60Au and S90Au for bottom images. (b) (left) Schematic illustration of the distance between the hot spot center and its neighboring Au NP surface, d_{hs}, and the deviation angle between the NP center-to-hot spot line and the NP center-to-center axis, θ_h. (right) The plot of the log(EF) versus the horizontal distance corresponding to the white dashed line in the lower panel of (a) for each Au NP monolayer. The vertical gray dashed line is tangential to the nearest NP surface. (c) Horizontal line profile of log(EF) versus the horizontal position of each Au NP monolayer corresponding to the black dotted line in (a) lower panel, with inset representing the log(EF) mapping of the corresponding region for each sample. The vertical dashed line indicates the closest NP edge-to-edge distance position for each sample.

DOI: 10.1021/acsami.7b01121
ACS Appl. Mater. Interfaces 2017, 9, 13457−13470

wavelength. A recent study by Wei et al. shows that the EF of periodic arrays of nano objects was determined by the nanostructure D/d_{gap} ratio.[45] This is because the value of D/d_{gap} determines both intensities of the LSPR and cross-section area of the analyte molecules. They developed an analytical model based on the Drude free-electron response assumption to calculate the maximum EM in an Au NP array, which is written as[45]

$$EF_{Drude}^{max} \cong (3\pi/2)\omega_p{}^4\varepsilon_d{}^{-2}\omega_\tau{}^{-3}\omega_{res}{}^{-1} \quad (5)$$

where ω_p is the plasma frequency of the Au NP film ($\omega_p = 2.25 \times 10^{15}$ Hz) and ω_τ is the relaxation frequency of an Au NP ($\omega_\tau = 7.254 \times 10^{12}$ Hz).[45] The resonance frequency, ω_{res}, is defined as

$$\omega_{res} \approx \omega_p(D/d_{gap}\varepsilon_d)^{-1/2} \quad (6)$$

with the dielectric constant, ε_d, of the Au NP film related to the real part of the complex dielectric function (ε_m') of the gold by $\varepsilon_d \approx -(D/d_{gap})/\varepsilon_m'$, with $\varepsilon_m' = -23.1$.[39] The log value of calculated maximum EF is 7.35 for S13Au film, 8.95 for S40Au film, 8.46 for S60Au film, and 9.52 for S90Au film. These values are in good agreement with their FDTD simulated counterparts (Figure 8d), except for a 2-order-of-magnitude difference between the EF of S13Au film calculated by the Drude model and by the FDTD simulation. This discrepancy for the S13Au film might be due to the fact that the Drude model did not take into account the individual NP size. It is worth mentioning that the experimental EFs are at least 1 order of magnitude lower than the Drude model for all NP sizes and the FDTD simulation for all sizes except 13 nm. The major contribution to this gap is that the experimental EFs are from averaged EM intensity across the Au NP monolayers, whereas the simulated and calculated counterparts are the maximum EFs (at discrete hot spots for the simulation). Effort to calculate average EM intensity from simulation results and investigation of Au NP multilayers is ongoing.

CONCLUSIONS

We have demonstrated a fast, simple, yet effective self-assembly technique to fabricate large Au NPs (>15 nm) into functional monolayers. This technique includes a water/oil/air three-phase system. A commercialized alkylamine ligand was successfully used to stabilize the self-assembled Au NP at a fixed separation distance. The main SPR band red-shifts and broadens with the increasing NP size for the Au NP monolayers. The near field intensity of the SPR is greatly enhanced in Au NP monolayers due to the coupling among NPs. As demonstrated in this study, Au NP monolayers with large D/d_{gap} have extremely high Raman sensitivity (EF up to 10^7), good spatial homogeneity (millimeter scale), long-term stability (up to 8 months), decent quantifying accuracy, and versatile SERS capability to probe more than one type of molecule. The FDTD simulation depicts that the maximum EF distributes close to NP surface (less than 3 nm) in the vicinity of the interparticle axis, whereas reduced EF regions exist in all Au NP films close to the interparticle gap of which the interparticle axis is orthogonal to the polarization vector of the incident light. The EFs evaluated by the experiments agrees fairly well with the FDTD simulated results as well as those calculated by the Drude model. Since the driving force for the formation of Au NP monolayers at the water/air interface is the minization of the system Helmholtz energy, our method should be NP size and shape insensitive. Therefore, it should be readily applied to assembly of other nanostructures into 2D functional thin films. This study is expected to open a new avenue in designing and fabricating the next-generation plasmonic devices based on the metallic nanoparticle thin films.

METHODS

Materials. See the Supporting Information for details.

Au NP Synthesis. See the Supporting Information for details. To produce aqueous 13 nm Au NP colloid (denoted as S13Au), a revised Turkevich method was employed as reported elsewhere.[77,78] Au NPs of larger sizes (S40Au, S60Au, and S90Au) were synthesized using a seeded growth method.[79]

Au NP Monolayer Self-Assembly. A revised three-phase self-assembly method was used to fabricate Au NP monolayers.[39] Briefly, 4 mL of octadecylamine ($C18\text{-}NH_2$)/organic solution (hexane/chloroform 1:1 by volume) was placed in a Petri dish bottom ($\Phi = 55$ mm). Then 0.3 mL of aqueous Au NP colloid was slowly injected into the organic solution. The colloidal drop protruded through the organic phase to form an air/water/oil triphase. Here we define hexane/chloroform/$C18\text{-}NH_2$ mixture as an oil phase. Afterward, 0.35 mL of ethanol was added to the oil phase at 0.06 mL/min. Golden-sheen-like Au NP islands gradually appeared at the water/oil interface and soon moved to water/air interface to form an Au NP monolayer. The process took less than 10 min. The film was transferred to solid wafers using a "drain-to-deposit" strategy reported elsewhere.[20] An optimized molar concentration of $C18\text{-}NH_2$ was used for each particle size. If all ligands were to attach to Au NP surfaces, the molar concentrations would equate to a maximum areal ligand density of 17.5 molecules/nm^2 for S13Au, 4.1 molecules/nm^2 for S40Au, 5.2 molecules/nm^2 for S60Au, and 5.0 molecules/nm^2 for S90Au. The larger optimal areal density for S13Au can be explained by the fact that smaller nanoparticles have larger curvature that allows for more dense grafting of ligands.

Characterization. See Supporting Information for details. The Au NP films were deposited on glass slides for ultraviolet−visible−near-infrared (UV−vis−NIR) spectroscopy, on silicon wafers for scanning electron microscopy (SEM), atomic force microscopy (AFM), and Raman spectroscopy, and on carbon-coated copper grids for transmission electron microscopy (TEM).

Finite-Difference Time Domain (FDTD) Simulations. The scattering and absorption analysis of *aqueous dispersions* of the Au NP colloids was performed using 2D FDTD simulations (Lumerical Solutions, Inc.). Since the aqueous dispersions were dilute, the Au NPs can be considered isolated. Therefore, a single Au sphere was simulated for each size. The diameter was set to the average experimental value, listed in Table 1. The refractive index of the surrounding media was set as 1.33 (for water at room temperature). The total-field scattered-field (TFSF) was used as the incident light,[80] and the boundary conditions of simulated field were set as perfectly matched layers.[39] The mesh size was set as 0.1 nm for S13Au and 0.25 nm for the other samples.

The EM field distribution in the Au NP *monolayers* was simulated using a three-dimensional (3D) FDTD method, similar to what has been reported.[39] A plane wave source (785 nm wavelength) with polarization vector, *E*, and propagation vector, *K*, was incident on a set of 15 Au NPs with periodic boundary conditions. The average particle size and interparticle space of each FDTD model was set the same as those analyzed by TEM (Table 1). The mesh size was set at 0.1 nm for S13Au, 0.30 nm for S40Au, 0.60 nm for S60Au, and 0.80 nm for S90Au.

ASSOCIATED CONTENT

Supporting Information

The Supporting Information is available free of charge on the ACS Publications website at DOI: 10.1021/acsami.7b01121.

Figures S1−S3 and Tables S1−S5 (PDF)

DOI: 10.1021/acsami.7b01121
ACS Appl. Mater. Interfaces 2017, 9, 13457−13470

AUTHOR INFORMATION

Corresponding Author

*E-mail: dhallinan@fsu.edu.

ORCID

Jagjit Nanda: 0000-0002-6875-0057

Daniel T. Hallinan Jr.: 0000-0002-3819-0992

Notes

The authors declare no competing financial interest.

ACKNOWLEDGMENTS

This manuscript has been authored by UT-Battelle, LLC under Contract No. DE-AC05-00OR22725 with the U.S. Department of Energy. The United States Government retains and the publisher, by accepting the article for publication, acknowledges that the United States Government retains a non-exclusive, paid-up, irrevocable, world-wide license to publish or reproduce the published form of this manuscript, or allow others to do so, for United States Government purposes. The Department of Energy will provide public access to these results of federally sponsored research in accordance with the DOE Public Access Plan (http://energy.gov/downloads/doe-public-access-plan). We are grateful for the start-up funding supplied by the Florida State University and the FAMU-FSU College of Engineering. This research was partially sponsored by the Laboratory Directed Research and Development Program of Oak Ridge National Laboratory, managed by UT-Battelle, LLC, for the U.S. Department of Energy. We acknowledge Y. Su and Y. Xin for support in TEM at the National High Magnetic Field Laboratory (TEM is supported by National Science Foundation Cooperative Agreement No. DMR-1157490 and No. DMR-0654118 and the State of Florida). We thank R. Liang, J. G. Park, and P. T. Hoang for the Raman spectroscopy support. We thank B. Ma and Y. Tian for support in UV−vis−NIR measurement. We thank Z. Wang, J. Xia, and J. Guan for the fruitful discussion on SERS. We thank I. Ivanov for fruitful discussions on UV−vis−NIR spectroscopy and SERS.

REFERENCES

(1) Fleischmann, M.; Hendra, P. J.; McQuillan, A. Raman Spectra of Pyridine Adsorbed at a Silver Electrode. *Chem. Phys. Lett.* **1974**, *26*, 163−166.

(2) Nie, S.; Emory, S. R. Probing Single Molecules and Single Nanoparticles by Surface-Enhanced Raman Scattering. *Science* **1997**, *275*, 1102−1106.

(3) Li, H.; Mo, Y.; Pei, N.; Xu, X.; Huang, X.; Chen, L. Surface-Enhanced Raman Scattering Study on Passivating Films of Ag Electrodes in Lithium Batteries. *J. Phys. Chem. B* **2000**, *104*, 8477−8480.

(4) Hartman, T.; Wondergem, C. S.; Kumar, N.; van den Berg, A.; Weckhuysen, B. M. Surface-and Tip-Enhanced Raman Spectroscopy in Catalysis. *J. Phys. Chem. Lett.* **2016**, *7*, 1570−1584.

(5) Dasary, S. S.; Singh, A. K.; Senapati, D.; Yu, H.; Ray, P. C. Gold Nanoparticle Based Label-Free Sers Probe for Ultrasensitive and Selective Detection of Trinitrotoluene. *J. Am. Chem. Soc.* **2009**, *131*, 13806−13812.

(6) Sanles-Sobrido, M.; Exner, W.; Rodríguez-Lorenzo, L.; Rodríguez-González, B.; Correa-Duarte, M. A.; Álvarez-Puebla, R. A.; Liz-Marzán, L. M. Design of Sers-Encoded, Submicron, Hollow Particles through Confined Growth of Encapsulated Metal Nanoparticles. *J. Am. Chem. Soc.* **2009**, *131*, 2699−2705.

(7) Zhang, P.; Xia, J.; Wang, Z.; Guan, J. Gold Nanoparticle-Packed Microdisks for Multiplex Raman Labelling of Cells. *Nanoscale* **2014**, *6*, 8762−8768.

(8) Barhoumi, A.; Zhang, D.; Tam, F.; Halas, N. J. Surface-Enhanced Raman Spectroscopy of DNA. *J. Am. Chem. Soc.* **2008**, *130*, 5523−5529.

(9) Anker, J. N.; Hall, W. P.; Lyandres, O.; Shah, N. C.; Zhao, J.; Van Duyne, R. P. Biosensing with Plasmonic Nanosensors. *Nat. Mater.* **2008**, *7*, 442−453.

(10) Craig, A. P.; Franca, A. S.; Irudayaraj, J. Surface-Enhanced Raman Spectroscopy Applied to Food Safety. *Annu. Rev. Food Sci. Technol.* **2013**, *4*, 369−380.

(11) Stiles, P. L.; Dieringer, J. A.; Shah, N. C.; Van Duyne, R. P. Surface-Enhanced Raman Spectroscopy. *Annu. Rev. Anal. Chem.* **2008**, *1*, 601−626.

(12) Yang, G.; Hu, L.; Keiper, T. D.; Xiong, P.; Hallinan, D. T. Gold Nanoparticle Monolayers with Tunable Optical and Electrical Properties. *Langmuir* **2016**, *32*, 4022−4033.

(13) Ko, H.; Singamaneni, S.; Tsukruk, V. V. Nanostructured Surfaces and Assemblies as Sers Media. *Small* **2008**, *4*, 1576−1599.

(14) Yu, Q.; Guan, P.; Qin, D.; Golden, G.; Wallace, P. M. Inverted Size-Dependence of Surface-Enhanced Raman Scattering on Gold Nanohole and Nanodisk Arrays. *Nano Lett.* **2008**, *8*, 1923−1928.

(15) Diebold, E. D.; Peng, P.; Mazur, E. Isolating Surface-Enhanced Raman Scattering Hot Spots Using Multiphoton Lithography. *J. Am. Chem. Soc.* **2009**, *131*, 16356−16357.

(16) Brolo, A. G.; Arctander, E.; Gordon, R.; Leathem, B.; Kavanagh, K. L. Nanohole-Enhanced Raman Scattering. *Nano Lett.* **2004**, *4*, 2015−2018.

(17) Fu, Q.; Zhan, Z.; Dou, J.; Zheng, X.; Xu, R.; Wu, M.; Lei, Y. Highly Reproducible and Sensitive Sers Substrates with Ag Inter-Nanoparticle Gaps of 5 Nm Fabricated by Ultrathin Aluminum Mask Technique. *ACS Appl. Mater. Interfaces* **2015**, *7*, 13322−13328.

(18) Romo-Herrera, J. M.; Alvarez-Puebla, R. A.; Liz-Marzán, L. M. Controlled Assembly of Plasmonic Colloidal Nanoparticle Clusters. *Nanoscale* **2011**, *3*, 1304−1315.

(19) Kodiyath, R.; Malak, S. T.; Combs, Z. A.; Koenig, T.; Mahmoud, M. A.; El-Sayed, M. A.; Tsukruk, V. V. Assemblies of Silver Nanocubes for Highly Sensitive Sers Chemical Vapor Detection. *J. Mater. Chem. A* **2013**, *1*, 2777−2788.

(20) Yang, G.; Hallinan, D. T., Jr. Self-Assembly of Large-Scale Crack-Free Gold Nanoparticle Films Using a 'Drain-to-Deposit' Strategy. *Nanotechnology* **2016**, *27*, 225604.

(21) Wang, Y. W.; Kao, K. C.; Wang, J. K.; Mou, C. Y. Large-Scale Uniform Two-Dimensional Hexagonal Arrays of Gold Nanoparticles Templated from Mesoporous Silica Film for Surface-Enhanced Raman Spectroscopy. *J. Phys. Chem. C* **2016**, *120*, 24382−24388.

(22) Park, Y.-K.; Yoo, S.-H.; Park, S. Assembly of Highly Ordered Nanoparticle Monolayers at a Water/Hexane Interface. *Langmuir* **2007**, *23*, 10505−10510.

(23) Chen, H. Y.; Lin, M. H.; Wang, C. Y.; Chang, Y. M.; Gwo, S. Large-Scale Hot Spot Engineering for Quantitative Sers at the Single-Molecule Scale. *J. Am. Chem. Soc.* **2015**, *137*, 13698−13705.

(24) Freeman, R. G.; Grabar, K. C.; Allison, K. J.; Bright, R. M.; et al. Self-Assembled Metal Colloid Monolayers: An Approach to Sers Substrates. *Science* **1995**, *267*, 1629−1632.

(25) Liu, S.; Zhu, T.; Hu, R.; Liu, Z. Evaporation-Induced Self-Assembly of Gold Nanoparticles into a Highly Organized Two-Dimensional Array. *Phys. Chem. Chem. Phys.* **2002**, *4*, 6059−6062.

(26) Adams, S. M.; Campione, S.; Capolino, F.; Ragan, R. Directing Cluster Formation of Au Nanoparticles from Colloidal Solution. *Langmuir* **2013**, *29*, 4242−4251.

(27) Trau, M.; Saville, D.; Aksay, I. Assembly of Colloidal Crystals at Electrode Interfaces. *Langmuir* **1997**, *13*, 6375−6381.

(28) Genson, K. L.; Holzmueller, J.; Jiang, C.; Xu, J.; Gibson, J. D.; Zubarev, E. R.; Tsukruk, V. V. Langmuir-Blodgett Monolayers of Gold Nanoparticles with Amphiphilic Shells from V-Shaped Binary Polymer Arms. *Langmuir* **2006**, *22*, 7011−7015.

(29) Bigioni, T. P.; Lin, X.-M.; Nguyen, T. T.; Corwin, E. I.; Witten, T. A.; Jaeger, H. M. Kinetically Driven Self Assembly of Highly Ordered Nanoparticle Monolayers. *Nat. Mater.* **2006**, *5*, 265−270.

DOI: 10.1021/acsami.7b01121
ACS Appl. Mater. Interfaces 2017, 9, 13457−13470

(30) Badia, A.; Cuccia, L.; Demers, L.; Morin, F.; Lennox, R. B. Structure and Dynamics in Alkanethiolate Monolayers Self-Assembled on Gold Nanoparticles: A DSC, FtT-IR, and Deuterium Nmr Study. *J. Am. Chem. Soc.* **1997**, *119*, 2682−2692.
(31) Kim, B.; Tripp, S. L.; Wei, A. Self-Organization of Large Gold Nanoparticle Arrays. *J. Am. Chem. Soc.* **2001**, *123*, 7955−7956.
(32) Jana, N. R.; Pal, T. Anisotropic Metal Nanoparticles for Use as Surface-Enhanced Raman Substrates. *Adv. Mater.* **2007**, *19*, 1761−1765.
(33) Wei, A.; Kim, B.; Sadtler, B.; Tripp, S. L. Tunable Surface-Enhanced Raman Scattering from Large Gold Nanoparticle Arrays. *ChemPhysChem* **2001**, *2*, 743−745.
(34) Le Ru, E. C.; Etchegoin, P. G. Single-Molecule Surface-Enhanced Raman Spectroscopy. *Annu. Rev. Phys. Chem.* **2012**, *63*, 65−87.
(35) Park, Y.-K.; Park, S. Directing Close-Packing of Midnanosized Gold Nanoparticles at a Water/Hexane Interface. *Chem. Mater.* **2008**, *20*, 2388−2393.
(36) Sugawa, K.; Akiyama, T.; Tanoue, Y.; Harumoto, T.; Yanagida, S.; Yasumori, A.; Tomita, S.; Otsuki, J. Particle Size Dependence of the Surface-Enhanced Raman Scattering Properties of Densely Arranged Two-Dimensional Assemblies of Au(Core)-Ag(Shell) Nanospheres. *Phys. Chem. Chem. Phys.* **2015**, *17*, 21182−21189.
(37) Tanoue, Y.; Sugawa, K.; Yamamuro, T.; Akiyama, T. Densely Arranged Two-Dimensional Silver Nanoparticle Assemblies with Optical Uniformity over Vast Areas as Excellent Surface-Enhanced Raman Scattering Substrates. *Phys. Chem. Chem. Phys.* **2013**, *15*, 15802−15805.
(38) Guo, Q.-H.; Zhang, C.-J.; Wei, C.; Xu, M.-M.; Yuan, Y.-X.; Gu, R.-A.; Yao, J.-L. Controlling Dynamic SERS Hot Spots on a Monolayer Film of Fe_3O_4@ Au Nanoparticles by a Magnetic Field. *Spectrochim. Acta, Part A* **2016**, *152*, 336−342.
(39) Yang, G.; Hallinan, D. T. Gold Nanoparticle Monolayers from Sequential Interfacial Ligand Exchange and Migration in a Three-Phase System. *Sci. Rep.* **2016**, *6*, 35339.
(40) Reincke, F.; Hickey, S. G.; Kegel, W. K.; Vanmaekelbergh, D. Spontaneous Assembly of a Monolayer of Charged Gold Nanocrystals at the Water/Oil Interface. *Angew. Chem., Int. Ed.* **2004**, *43*, 458−462.
(41) Reincke, F.; Kegel, W. K.; Zhang, H.; Nolte, M.; Wang, D.; Vanmaekelbergh, D.; Möhwald, H. Understanding the Self-Assembly of Charged Nanoparticles at the Water/Oil Interface. *Phys. Chem. Chem. Phys.* **2006**, *8*, 3828−3835.
(42) Binks, B. P. Particles as Surfactants—Similarities and Differences. *Curr. Opin. Colloid Interface Sci.* **2002**, *7*, 21−41.
(43) Pieranski, P. Two-Dimensional Interfacial Colloidal Crystals. *Phys. Rev. Lett.* **1980**, *45*, 569−572.
(44) Jasper, J. J. The Surface Tension of Pure Liquid Compounds. *J. Phys. Chem. Ref. Data* **1972**, *1*, 841−1010.
(45) Genov, D. A.; Sarychev, A. K.; Shalaev, V. M.; Wei, A. Resonant Field Enhancements from Metal Nanoparticle Arrays. *Nano Lett.* **2004**, *4*, 153−158.
(46) Nordlander, P.; Oubre, C.; Prodan, E.; Li, K.; Stockman, M. Plasmon Hybridization in Nanoparticle Dimers. *Nano Lett.* **2004**, *4*, 899−903.
(47) Jain, P. K.; Huang, W.; El-Sayed, M. A. On the Universal Scaling Behavior of the Distance Decay of Plasmon Coupling in Metal Nanoparticle Pairs: A Plasmon Ruler Equation. *Nano Lett.* **2007**, *7*, 2080−2088.
(48) Huang, X.; El-Sayed, M. A. Gold Nanoparticles: Optical Properties and Implementations in Cancer Diagnosis and Photothermal Therapy. *J. Adv. Res.* **2010**, *1*, 13−28.
(49) Taz, H.; Ruther, R.; Malasi, A.; Yadavali, S.; Carr, C.; Nanda, J.; Kalyanaraman, R. In Situ Localized Surface Plasmon Resonance (Lspr) Spectroscopy to Investigate Kinetics of Chemical Bath Deposition of Cds Thin Films. *J. Phys. Chem. C* **2015**, *119*, 5033−5039.
(50) Jain, P. K.; Lee, K. S.; El-Sayed, I. H.; El-Sayed, M. A. Calculated Absorption and Scattering Properties of Gold Nanoparticles of Different Size, Shape, and Composition: Applications in Biological Imaging and Biomedicine. *J. Phys. Chem. B* **2006**, *110*, 7238−7248.
(51) Mie, G. Beiträge Zur Optik Trüber Medien, Speziell Kolloidaler Metallösungen. *Ann. Phys.* **1908**, *330*, 377−445.
(52) Kreibig, U.; Vollmer, M. Theoretical Considerations. In *Optical Properties of Metal Clusters*; Springer: 1995; pp 13−201.
(53) Muskens, O.; Giannini, V.; Sánchez-Gil, J.; Gómez Rivas, J. Optical Scattering Resonances of Single and Coupled Dimer Plasmonic Nanoantennas. *Opt. Express* **2007**, *15*, 17736−17746.
(54) Muskens, O.; Giannini, V.; Sanchez-Gil, J.; Gomez Rivas, J. Strong Enhancement of the Radiative Decay Rate of Emitters by Single Plasmonic Nanoantennas. *Nano Lett.* **2007**, *7*, 2871−2875.
(55) Hao, F.; Larsson, E. M.; Ali, T. A.; Sutherland, D. S.; Nordlander, P. Shedding Light on Dark Plasmons in Gold Nanorings. *Chem. Phys. Lett.* **2008**, *458*, 262−266.
(56) Shafiei, F.; Monticone, F.; Le, K. Q.; Liu, X. X.; Hartsfield, T.; Alu, A.; Li, X. Q. A Subwavelength Plasmonic Metamolecule Exhibiting Magnetic-Based Optical Fano Resonance. *Nat. Nanotechnol.* **2013**, *8*, 95−99.
(57) Gwo, S.; Chen, H. Y.; Lin, M. H.; Sun, L. Y.; Li, X. Q. Nanomanipulation and Controlled Self-Assembly of Metal Nanoparticles and Nanocrystals for Plasmonics. *Chem. Soc. Rev.* **2016**, *45*, 5672−5716.
(58) Campion, A.; Kambhampati, P. Surface-Enhanced Raman Scattering. *Chem. Soc. Rev.* **1998**, *27*, 241−250.
(59) Kagan, M. R.; McCreery, R. L. Reduction of Fluorescence Interference in Raman Spectroscopy Via Analyte Adsorption on Graphitic Carbon. *Anal. Chem.* **1994**, *66*, 4159−4165.
(60) Maher, R. C.; Dalley, M.; Le Ru, E. C.; Cohen, L. F.; Etchegoin, P. G.; Hartigan, H.; Brown, R. J. C.; Milton, M. J. T. Physics of Single Molecule Fluctuations in Surface Enhanced Raman Spectroscopy Active Liquids. *J. Chem. Phys.* **2004**, *121*, 8901−8910.
(61) Le Ru, E. C.; Etchegoin, P. G. Rigorous Justification of the E (4) Enhancement Factor in Surface Enhanced Raman Spectroscopy. *Chem. Phys. Lett.* **2006**, *423*, 63−66.
(62) Lewis, I. R.; Edwards, H. *Handbook of Raman Spectroscopy: From the Research Laboratory to the Process Line*; CRC Press: 2001.
(63) Liu, J. W.; Zhang, S. Y.; Qi, H.; Wen, W. C.; Yu, S. H. A General Strategy for Self-Assembly of Nanosized Building Blocks on Liquid/Liquid Interfaces. *Small* **2012**, *8*, 2412−2420.
(64) Lee, H. K.; Lee, Y. H.; Zhang, Q.; Phang, I. Y.; Tan, J. M. R.; Cui, Y.; Ling, X. Y. Superhydrophobic Surface-Enhanced Raman Scattering Platform Fabricated by Assembly of Ag Nanocubes for Trace Molecular Sensing. *ACS Appl. Mater. Interfaces* **2013**, *5*, 11409−11418.
(65) Kim, K.; Han, H. S.; Choi, I.; Lee, C.; Hong, S.; Suh, S.-H.; Lee, L. P.; Kang, T. Interfacial Liquid-State Surface-Enhanced Raman Spectroscopy. *Nat. Commun.* **2013**, *4*, 2182.
(66) Rey, I.; Johansson, P.; Lindgren, J.; Lassegues, J.; Grondin, J.; Servant, L. Spectroscopic and Theoretical Study of (CF3SO2)2n-(TFSI-) and (CF3SO2) 2NH(HTFSI). *J. Phys. Chem. A* **1998**, *102*, 3249−3258.
(67) Howlett, P.; Brack, N.; Hollenkamp, A.; Forsyth, M.; MacFarlane, D. Characterization of the Lithium Surface in N-Methyl-N-Alkylpyrrolidinium Bis (Trifluoromethanesulfonyl) Amide Room-Temperature Ionic Liquid Electrolytes. *J. Electrochem. Soc.* **2006**, *153*, A595−A606.
(68) Bednarska-Bolek, B.; Jakubas, R.; Bator, G.; Baran, J. Vibrational Study of the Structural Phase Transition in Bis (Pyrrolidinium)-Chloride-Hexachloroantimonate (V) by Infrared Spectroscopy. *J. Mol. Struct.* **2002**, *614*, 151−157.
(69) Jaworska, A.; Wojcik, T.; Malek, K.; Kwolek, U.; Kepczynski, M.; Ansary, A. A.; Chlopicki, S.; Baranska, M. Rhodamine 6g Conjugated to Gold Nanoparticles as Labels for Both SERS and Fluorescence Studies on Live Endothelial Cells. *Microchim. Acta* **2015**, *182*, 119−127.
(70) Giorgini, M. G.; Futamatagawa, K.; Torii, H.; Musso, M.; Cerini, S. Solvation Structure around the Li+ Ion in Mixed Cyclic/Linear Carbonate Solutions Unveiled by the Raman Noncoincidence Effect. *J. Phys. Chem. Lett.* **2015**, *6*, 3296−3302.

DOI: 10.1021/acsami.7b01121
ACS Appl. Mater. Interfaces 2017, 9, 13457−13470

(71) Etchegoin, P. G.; Le Ru, E. A Perspective on Single Molecule SERS: Current Status and Future Challenges. *Phys. Chem. Chem. Phys.* **2008**, *10*, 6079−6089.
(72) Zhao, L. L.; Kelly, K. L.; Schatz, G. C. The Extinction Spectra of Silver Nanoparticle Arrays: Influence of Array Structure on Plasmon Resonance Wavelength and Width. *J. Phys. Chem. B* **2003**, *107*, 7343−7350.
(73) Hooshmand, N.; Panikkanvalappil, S. R.; El-Sayed, M. A. Effects of the Substrate Refractive Index, the Exciting Light Propagation Direction, and the Relative Cube Orientation on the Plasmonic Coupling Behavior of Two Silver Nanocubes at Different Separations. *J. Phys. Chem. C* **2016**, *120*, 20896−20904.
(74) Moskovits, M. Surface-Enhanced Raman Spectroscopy: A Brief Retrospective. *J. Raman Spectrosc.* **2005**, *36*, 485−496.
(75) Bryant, G. W.; García de Abajo, F. J.; Aizpurua, J. Mapping the Plasmon Resonances of Metallic Nanoantennas. *Nano Lett.* **2008**, *8*, 631−636.
(76) Xu, H.; Aizpurua, J.; Käll, M.; Apell, P. Electromagnetic Contributions to Single-Molecule Sensitivity in Surface-Enhanced Raman Scattering. *Phys. Rev. E: Stat. Phys., Plasmas, Fluids, Relat. Interdiscip. Top.* **2000**, *62*, 4318.
(77) Yang, G.; Chang, W.-S.; Hallinan, D. T. A Convenient Phase Transfer Protocol to Functionalize Gold Nanoparticles with Short Alkylamine Ligands. *J. Colloid Interface Sci.* **2015**, *460*, 164−172.
(78) Turkevich, J.; Stevenson, P. C.; Hillier, J. The Size and Shape Factor in Colloidal Systems. *Discuss. Faraday Soc.* **1951**, *11*, 55.
(79) Ziegler, C.; Eychmüller, A. Seeded Growth Synthesis of Uniform Gold Nanoparticles with Diameters of 15−300 Nm. *J. Phys. Chem. C* **2011**, *115*, 4502−4506.
(80) Umashankar, K.; Taflove, A. A Novel Method to Analyze Electromagnetic Scattering of Complex Objects. *IEEE Trans. Electromagn. Compat.* **1982**, *EMC-24*, 397−405.
(81) Creighton, J. A.; Blatchford, C. G.; Albrecht, M. G. Plasma Resonance Enhancement of Raman Scattering by Pyridine Adsorbed on Silver or Gold Sol Particles of Size Comparable to the Excitation Wavelength. *J. Chem. Soc., Faraday Trans. 2* **1979**, *75*, 790−798.

DOI: 10.1021/acsami.7b01121
ACS Appl. Mater. Interfaces 2017, 9, 13457−13470